

# INITIAL RESULTS FROM SECIS OBSERVATIONS OF THE 2001 ECLIPSE

A.C. Katsiyannis<sup>(1)</sup>, R.T.J. McAteer<sup>(1)</sup>, D.R. Williams<sup>(2,1)</sup>, P.T. Gallagher<sup>(3)</sup>, F.P. Keenan<sup>(1)</sup>

<sup>(1)</sup>*Department of Pure and Applied Physics, Queen's University Belfast, Belfast, BT7 1NN, U.K.,  
a.katsiyannis@qub.ac.uk and j.mcateer@qub.ac.uk and f.keenan@qub.ac.uk*

<sup>(2)</sup>*Mullard Space Science Laboratory, University College London, Holmbury St. Mary, Dorking, Surrey, RH5 6NT, U.K.,  
drw@mssl.ucl.ac.uk*

<sup>(3)</sup>*L-3 Communications GSI, NASA Goddard Space Flight Center, Greenbelt, MD 20771, U.S.A.,  
Peter.T.Gallagher@hessi.gsfc.nasa.gov*

## ABSTRACT

SECIS observations of the June 2001 total solar eclipse were taken using an Fe XIV 5303 Å filter. Existing software was modified and new code was developed for the reduction and analysis of these data. The observations, data reduction, study of the atmospheric and instrumental effects, together with some preliminary results are discussed. Emphasis is given to the techniques used for the automated alignment of the 8000 images, the application of the à Trous algorithm for noise filtering and the software developed for the automated detection of intensity oscillations using wavelet analysis. In line with findings from the 1999 SECIS total eclipse observations, intensity oscillations with periods in the range of 20-30 s, both inside and just outside coronal loops are also presented.

## 1. INTRODUCTION

Coronal loops are known to be subject to different types of magnetohydrodynamic (MHD) oscillations. Review papers by Aschwanden et al. [1], Nakariakov [2], Roberts [3] and others provide an overview of the theoretical and observational progress on the detection of such oscillations in solar coronal loops. It is believed that the study of those events may provide us with more information about the physical characteristics of the corona (a subject area called coronal seismology) and help us investigate the feasibility of the coronal oscillations as a corona heating mechanism.

It has been suggested that MHD waves can be divided into two main categories. Magnetoacoustic waves, consisting of density, pressure and temperature perturbations (which in turn are divided into slow and fast modes) and incompressible Alfvén waves (which are also divided into those with movements perpendicular to the magnetic field and the torsional oscillations). Roberts et al. [4] provide a detailed theoretical study, using reasonable approximations for a low- $\beta$  plasma, of the fast-mode magneto-

acoustic perturbations and predict that fast magnetoacoustic (sausage-mode) oscillations with periodicity of  $\sim 1$  Hz may be excited in coronal loops. The same authors also predict how the signature of a wave train, created by a pulsation and propagating to a distance  $h$  from its source, could provide us with information of the physical parameters of the loop. More recently Nakariakov et al. [5] have confirmed the analytical work of Roberts et al. [4] on the propagation of wave trains, by numerically modelling a perturbing pulse and simulating the time series as developed at a distance  $h$  along the loop.

The coronal heating problem is addressed by a large number of authors with two main mechanisms proposed as the most likely explanation (see review article by Priest & Schrijver [6]). One of these is that a large number of magnetic reconnections causing current dissipation could result in micro- or nano-flare activity on a regular basis (see Parker [7] for further discussion). The other suggestion is the damping of MHD waves, caused by ion viscosity and electrical resistivity (first introduced by Hollweg [8]).

Following a long sequence of attempts to detect coronal oscillations using total solar eclipse observations (Koutchmy et al. [9], Pasachoff & Landman [10], Singh et al. [11], Cowsik et al. [12], Pasachoff et al. [13]), the Solar Eclipse Coronal Imaging System (SECIS) observed the 1999 total solar eclipse using an Fe XIV 5303 Å filter. Phillips et al. [14] developed SECIS and used the instrument to observe the total solar eclipses of 1999 and 2001. They succeeded in detecting several periodicities in the range of 4-7 s (Williams et al. [15], Williams et al. [16], Katsiyannis et al. [17]) in the 1999 data set. A propagating wave train was detected by [16] with a phase-speed of  $\sim 2100 \text{ km s}^{-1}$ , reinforcing the identification of this perturbation as a fast-mode MHD wave. Considering the physical parameters of the loop (physical dimensions, density, etc) and making reasonable assumptions about the strength of the magnetic field, it was found that the frequencies detected are well within the range of predicted values in [4]. Work on different loops in the same active region [17] failed to detect a wave train but found

intensity oscillations just outside these loops. These perturbations were in the same frequency range as those detected by [16] and with similar amplitudes.

In this paper we discuss observations taken during the June 2001 total solar eclipse, the reduction and data analysis techniques developed to process these data and some preliminary detections of oscillations in the lower solar coronal.

## 2. OBSERVATIONS

For a detail description of the instrument and details of the August 1999 observations, see [14]. Since the previous eclipse, several alterations were made to the system, to improve the performance of the instrument.

- A broader, Fe XIV 5303 Å filter was used. While both filters were centred on the 5303 Å line, the previous filter had full-width-half-maximum (FWHM) of 2 Å while the new filter has a FWHM of 5 Å.
- A metallic cover was produced to seal the optical elements of SECIS from scattered light. The area covered extended from the back of the Schmidt telescope to the charge-coupled device (CCD) cameras (see [14] for more details on the instrument layout).
- The driving mechanism of the heliostat was covered to protect against particles of dust or mud. This was considered important as any contamination could cause a temporarily change of the rotation speed of the heliostat.
- Cooling fans were installed on the CCD cameras to minimize high temperature effects.

Similar procedures to the August 1999 observations were followed for the 21 June 2001 total solar eclipse. The instrument was located on the roof of the physics department of the University of Zambia, in Lusaka, Zambia (Latitude: 15° 20' South; Longitude: 28° 14' East). The instrument was transported to the location in parts and assembled on the spot a few days before the eclipse. The heliostat was aligned to the site's local meridian by using the standard gnomon technique. The optical components were aligned using a small pocket laser and the instrument was focused using very distant objects. On the day of the eclipse weather conditions were very good, with practically no wind nor clouds. The cooling fans were switched on early in the morning of the eclipse, but were switched off minutes before totality to avoid causing vibrations to the instrument.

The CCD detectors each have  $512 \times 512$  pixel<sup>2</sup>, which combined with the instrument's optics provide us with a resolution of  $\sim 4$  arcsec pixel<sup>-1</sup> (see [15] and references therein) and an observable area of  $\sim 34 \times 34$  arcmin<sup>2</sup>. As edge effects of the CCD prevent us from using all  $512 \times 512$  elements (only an area of  $\sim 400 \times 300$  pixel<sup>2</sup> is considered to be free of edge effects) and in line with the practice we followed during the 1999 total solar eclipse,

we decided not to observe the whole disk, but only the North-East limb. The choice of location was based on the appearance of NOAA Active Region 9513 on the limb of the disk in the same general area the previous day. Coordinated Solar and Heliospheric Observatory (SoHO) observations of the same area were taken during totality in order to provide us with the ability to determine the physical characteristics of any coronal regions detected with intensity oscillations. The SECIS instrument itself obtained 8000 images at a rate of 39 frames per second covering the whole duration of totality.

The next morning sky flats and dark frames were taken. For the sky flats we used the same exposure time as with the eclipse observations, while for the dark frames we covered the CCD cameras completely with a black cloth, closed the aperture of the lenses to f/22 and set the exposure time equal to that used during eclipse.

## 3. DATA REDUCTION AND ANALYSIS

As SECIS is a project-specific instrument, no data reduction software is widely available and with the exception of some subroutines written for the August 1999 observations, the subroutines used were developed from scratch. As some of the procedures applied are not commonly used in astronomical software, a detailed description follows below.

### 3.1. Image Alignment

The first part of the data reduction included dark current and sky flat subtraction performed as is normal for most astronomical observations. The next part of the reduction was less common in astronomical data reduction as the images had to be aligned with an accuracy of a fraction of a pixel in order to achieve the accuracy needed for the study of intensity oscillations. One of the difficulties was that, unlike the 1999 observations, no prominence was present on the limb of the sun at the time of the eclipse and hence the previous alignment procedure (see [15] for a detailed description) had to be modified. Although the first part of the alignment of the 2001 data set was very similar to that of the previous observations, the whole procedure will be described for completeness.

A first order approximation of the position of the lunar disk was achieved by using the Sobel filter to calculate the edge of the Moon on each individual frame. Then, assuming a constant lunar radius, a fit of the disk was produced by using the least square method and rejecting all points lying outside more than  $3\sigma$  outside the best fit. The next step was to assume the motion of the Moon with respect to the Sun was of constant angular velocity and thus aligning the images with an accuracy of  $\sim 1$  pixel.

For further accuracy in alignment, a second stage was introduced to the process. An area of a reference image containing featureless parts of the corona and with a sharp transition to the moon disk was identified and expanded by a factor of 20 along each axis. For the 8000

individual images, the same area was expanded by a factor of 20 and those areas were cross-correlated with the reference image. Then for every frame the pixel shift that gave the best correlation was divided by 20 and stored as the shift of that frame. The whole, unexpanded images were shifted by those values using bilinear interpolation for non-integer shifts. This procedure thus aligned the images to an accuracy of 0.05 pixel.

### 3.2. Wavelet analysis

A continuous wavelet transformation was used to analyse the observations described for two main reasons:

Firstly, wavelet algorithms have gradually started to replace the classical Fourier analysis as it provides us with localised temporal information. Coronal oscillations are not necessarily expected to last longer than a few periods, therefore high frequency oscillations with periodicities of a few seconds may not last longer than a few tens of seconds, i.e., much shorter than the  $\sim 3$  min of the SECIS 2001 observations. Fourier analysis has, by nature, a limited ability to detect oscillations lasting a fraction of the time series, making the wavelet analysis the method of choice. Torrence & Compo [18] have described in detail this algorithm and provided a discussion of the benefits of it's application on different scientific fields.

Secondly, the increased popularity of the wavelet transformation (for example, Gallagher et al. [19]; Ireland et al. [20]; Banerjee et al. [21]) and its consistent use throughout the analysis of the 1999 SECIS observations ([15], [16], [17]), make it an obvious choice as it allows us to make direct comparisons with recent work in this subject area.

A Morlet wavelet was used for the analysis of our data, with waveform

$$\psi(\eta) = \pi^{-1/4} \exp(i\omega_0\eta) \exp\left(\frac{-\eta^2}{2}\right), \quad (1)$$

where  $\eta = t/s$  is the dimensionless time parameter,  $t$  is the time,  $s$  the scale of the wavelet (i.e. its duration),  $\omega_0 = s\omega$  is the dimensionless frequency parameter, and  $\pi^{-1/4}$  is a normalization term (see [18]).

The results of the wavelet analysis as described above applied to the  $x=333$ ,  $y=187$  pixel of the aligned 2001 data set can be seen in Figure 1. It is divided into two areas with panel (a) showing the power density wavelet transform with the lighter areas representing the higher values. The hatched region marks the cone-of-influence (COI) and represents the areas that suffer from edge effects. Everything inside the COI is discarded for the purposes of this work. For further discussion on the edge effects introduced by a finite time-series see [18] and references therein. The contours of panel (a) surround the area where the detected power exceeds the 99% confidence level.

Panel (b) contains the global wavelet spectrum, which is the wavelet analogue of the standard Fourier transform. It

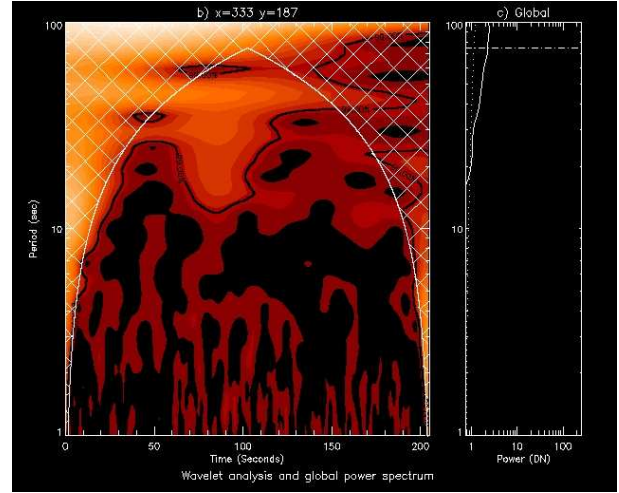


Figure 1. Wavelet transform analysis of point  $x=333$ ,  $y=187$  of the aligned data set. (a) contains the wavelet transform of the time series and (b) the global wavelet spectrum. The contours in panel (b) highlight the areas where the detected power is at the 99% confidence level and the hatched area, the cone-of-influence (COI).

is produced by summing the power density wavelet transform over the whole time series, while the dotted line running along the period axis is the global significance level (again summed over time) at the same value (99%) as the contours in panel (a). The horizontal dot-dashed line near the top of panel (b) marks the bottom of the COI and all detections below this frequency should be discarded.

### 3.3. Noise Reduction

SECIS has been designed as a highly portable and autonomous astronomical instrument, made to be able to observe in any location with a minimum of infrastructure requirements. As such, one of the most significant limitations of the instrument is that the 200 mm aperture of the Meade Schmidt-Cassegrain  $f/10$  telescope (see [14] for more details), in conjunction with the ultra-fast sampling rate of the cameras, results in a low signal-to-noise ratio (S/N).

Various noise reduction possibilities were investigated and the à Trous filtering was chosen as the optimal method. This is a standard mathematical procedure developed for any time-series affected by either Gaussian or Poisson noise, to be analysed by wavelet transformations. It is commonly applied to astronomical image and data analysis and readily available in literature. Starck & Murtagh [22] provide a detailed description of the method and its applications. The non-entropy-based variety of the à Trous method was chosen for simplicity.

The sequence of 8000 frames taken during the eclipse is, in effect, a three-dimensional array where the  $x$ ,  $y$  axes are the CCD's two dimensions and the  $z$  axis is the image number. This array can be divided into vectors (or time series) of the same  $x$ ,  $y$  location extending through the whole range of  $z$ . The 1-d à Trous algorithm can then be

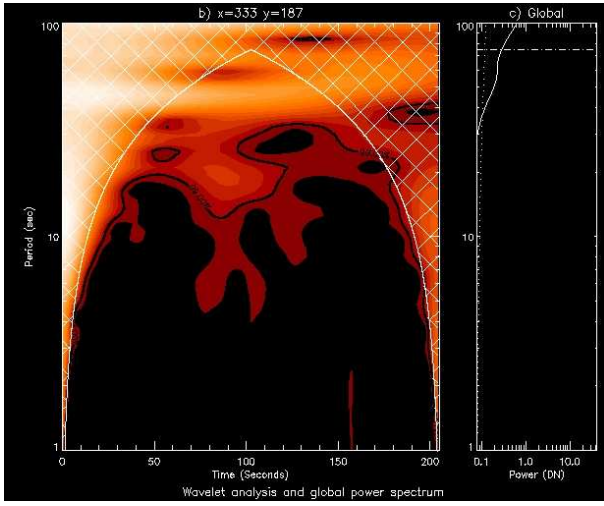


Figure 2. The wavelet analysis of the same point as in Figure 1 after being filtered through the  $\hat{\alpha}$  Trous algorithm.

applied to each such time series separately.

Figure 2 contains the results of the wavelet analysis of the  $x=333$ ,  $y=187$  pixel after filtering by the  $\hat{\alpha}$  Trous transformation. This is the same point analysed previously in Figure 1 and a comparison between the two will reveal the effect of the  $\hat{\alpha}$  Trous de-noising to the data set. The filtering has affected the power spectrum in two distinct ways, both of which can be associated with noise reduction.

Firstly, the lower the periodicity, the greater the reduction in power. For our example, practically all oscillations below 4 s have disappeared while those above 30 s are largely unaffected. This is compatible with noise reduction since it is well understood that noise tends to have a larger effect on frequencies that are closer to the sampling rate (i.e., high frequencies are more influenced by noise).

Second, the oscillation at around  $\sim 30$  s that, based on previous criteria (see [17] and discussion in next section), should be considered “real” (i.e., caused by intensity oscillations in the solar corona), is affected as expected. In particular, the duration of the oscillation remains practically unchanged (from the edge of the COI to 123<sup>rd</sup> second), while the span of the oscillation in the period axis has been reduced. This is again compatible with noise reduction as detections caused by noise tend to be very “elongated” on the period axis (i.e., have short duration but stretch along many periodicities).

Interestingly, the shape of the oscillation in the wavelet space after de-noising, bears a close resemblance to the theoretical prediction by [5]. They produced the wavelet analysis of a numerically created, impulsively, short-period magnetoacoustic wave train as it would have been observed while propagating at distance  $h$  from its source. Similarly to [5] simulations, the wavelet transformation of Figure 2 contains a narrow spectrum tail leading to a much broader band head (a “tadpole”).

#### 4. AUTOMATED DETECTION OF OSCILLATIONS

The main purpose of the SECIS observations is to detect coronal intensity oscillations. Although S/N limitations confine the search of such perturbations to the lower corona and more specifically in the areas around coronal loops, these areas are sufficiently large to require the development of software techniques to automatically detect such events throughout the whole data set. Additionally, the same piece of software will be used to deal with potential instrumental and atmospheric effects (see Section 5).

For consistency with previous work (mainly [16] and [17]) we implemented the following criteria for distinguishing between those detections that are due to noise and those that are caused by signal variations (either as a result of instrumental effects, the atmosphere, or genuine coronal intensity variations):

- All coefficients falling within the COI are discarded.
- Only those areas of a 99% confidence level or higher are taken into account.
- Oscillations lasting less than the time length of three periods are considered noise.

For a detailed discussion on the significance of these criteria, see [17]. A step-by-step description of the algorithm follows:

1. For a given pixel of the data set the 2-d wavelet coefficients of the time series is produced (as for Figures 2 and 3).
2. For the lowest periodicity of the analysis, the number of the first sample in time that is unaffected by the COI is determined. We call this sample  $t$ .
3. For the same periodicity the last sample that is unaffected by the COI,  $t'$ , was determined.
4. The number of the sample that predates  $t'$  by three periodicities is determined. We call this sample  $t_{max}$ .
5. The confidence level of the sample  $t$  is extracted.
6. If the confidence level is 99% or higher, then the confidence level of the sample that is three periods later than  $t$ , referred to here as  $t_{+3}$ , is also extracted. Otherwise we move to step 8.
7. If the confidence level of  $t_{+3}$  is also 99% or higher the co-ordinates of the pixel are recorded together with the current periodicity and  $t$ . In this case the algorithm moves to step no. 9. It is assumed that if  $t$  and  $t_{+3}$  have both confidence level of 99% or higher, all samples between them will have confidence level of 99% or higher in the same periodicity.
8. Move to the next  $t$  and repeat steps 5-7 until  $t$  becomes  $t_{max}$ .

9. Move to next periodicity and repeat steps 2-8 until the periodicity reaches the limit of 70.9 s.
10. Move to the next pixel of the array and start again from the beginning.

For periods of more than 70.9 s the part of the time series that is outside the COI is not longer than three periodicities. For such periods, the criteria established at the beginning of this section cannot therefore be satisfied.

## 5. INSTRUMENTAL AND ATMOSPHERIC EFFECTS

The field-of-view covered by the SECIS observations can be roughly divided into two areas. The first is covered by the lunar disk and contains no signal apart from that of scattered light from the atmosphere. The second area contains part of the lower corona and the signal is dominated by light from the Sun's atmosphere. The third part covers the outer corona and although most of the signal is again of solar origin, a significant portion of it is due to earth's atmosphere.

The automated method described in the previous sector was applied first to the area covered by the moon disk in order to assess the existence of instrumental and atmospheric oscillations. The signal recorded from that area can only be from the scattered light of the atmosphere and the CCD read-out noise, making it the most suitable tool for determining bogus oscillations in the data set. By analysing a rectangular area of  $200 \times 50$  pixel<sup>2</sup>,  $\sim 2000$  detections of oscillations were made across the whole spectrum of periodicities. We applied the same procedure in parts of the lower (covering an area of  $50 \times 250$  pixel<sup>2</sup>) and outer ( $50 \times 300$  pixel<sup>2</sup>) corona and found  $\sim 750$  and  $\sim 4000$  oscillations respectively. All three areas are a minimum of 100 pixels away from the left and right sides and 200 pixels away from the top and bottom of the image. This is because instrumental oscillations are known to appear in the edges of the CCD due to manufacturing limitations. Also, detections that started during the first 1000 frames as well as those that finished during the last 1000 frames were discarded as they may have been affected by light from the photosphere during the start or end of the eclipse (an effect also known as "diamond rings effect").

From the analysis of the above results it is apparent that a circular area centred at the bottom part of the edge of moon's disk has a very limited number of oscillations. A closer inspection revealed that this area of the CCD has saturated by photospheric diamond rings. The rest of the data set contains oscillations that are randomly scattered in space in all periodicities.

## 6. OSCILLATION DETECTIONS

From the areas of the lower corona analysed so far, the most interesting is the loop of AR 9513 displayed in red-scale in Figure 3. Marked with crosses are the pixels that

*Figure 3. Solar coronal loop of AR 9513 as observed by SECIS during the 2001 solar eclipse. The average intensity of the pixels is displayed with the red-scale. Marked with crosses are the pixel detected to oscillate in intensity according the criteria of section 4.*

have been detected with intensity oscillations with periods in the range of 20-30 s, while the units of the x and y axes are pixel co-ordinates of the aligned data set. With the existence of atmospheric and instrumental detections in the data set well established, it can be estimated that approximately two thirds of the detections of Figure 3 are likely to be of solar origin. This is for three main reasons:

- Compared to the nearby areas of the lunar disk and the outer corona which were scanned for oscillations, the area of Figure 3 contains  $\sim 3$  and 2 times more detections respectively. Whereas the number of oscillations per unit spatial area remains constant, regardless of the arbitrary area chosen, either on the lunar disk or in the outer corona, this is not the case for the area of lower corona presented in Figure 3.
- The spatial distribution of the oscillations is non-random. Again, this is distinct from all areas of the moon and the outer corona, with the only exception of the part of the data set affected by the instrumental limitations described above, have a random scatter of detections throughout the field.
- The detections of Figure 3 form a shape that approximately "coincides" with a coronal loop of AR 9513.

The results described above are compatible with those based on the SECIS 1999 observations as described by [15], [16], [17]. As seen in Figure 3, there are two important confirmations of previously published results. Firstly, there are intensity perturbations both inside and exactly outside visible coronal loops. This is in line with the findings of [15], [16] of oscillations inside and [17] of oscillations outside coronal loops. Secondly, as previously reported by [17], more intensity variations can be found outside the loops, towards the tenuous part of the

corona, than towards the denser part (i.e., more oscillations can be detected at the higher altitudes of the solar corona than the lower). For a more detailed discussion on this result see [17].

The results presented above confirm the SECIS ability to detect MHD oscillations and their presence in the data set of the 2001 observations. A detailed study of the detections reported above is to follow and more work will be done in extending the search for detections to other loops of AR 9513. Satellite observations of the same active region shortly before, during and just after the eclipse can be combined to determine various physical parameters useful in the interpretation of the SECIS 2001 observations.

## ACKNOWLEDGMENTS

The authors would like to thank K.J.H. Phillips for his collaboration on the SECIS project. PPARC funding was used during this work. ACK acknowledges the Leverhume Trust for funding via grant F00203/A. JMA & DRW thank DEL and QUB for studentships. FPK is grateful to AWE Aldermaston for the award of the William Penney fellowship.

## REFERENCES

1. Aschwanden M. J., Fletcher L., Schrijver C. J., Alexander D., *ApJ* 520, 880, 1999
2. Nakariakov V.M., in *Dynamic Sun*, Ed. B. Dwivedi, CUP, 2003
3. Roberts B., in Proc., 10th European Solar Physics Meeting, '*Solar Variability: From Core to Outer Frontiers*', ESA SP-506, 481, 2002
4. Roberts B., Edwin P.M., Benz A.O., 1984, *ApJ*, 279, 857
5. Nakariakov V.M., Arber T.D., Ault C.E., Katsiyannis A.C., Williams D.R., 2004, *MNRAS*, submitted
6. Priest, E.R. & Schrijver, C.J., 1999, *Sol. Phys.*, 190, 1
7. Parker, E.N., 1988, *ApJ*, 330, 474
8. Hollweg, J.V., 1981, *Sol. Phys.*, 70, 25
9. Koutchmy, S., Žugžda, Y.D. & Locăns, V., 1983, *A&A*, 120, 185
10. Pasachoff, J.M. & Landman, D.A., 1984, *Sol. Phys.*, 90, 325
11. Singh, J., Cowsik, R., Raveendran, A.V., Bagare, S.P., Saxena, A. K., Sundararaman, K., Krishan, V., Naidu, N., Samson, J.P. A., Gabriel, F., 1997, *Sol. Phys.*, 170, 235
12. Cowsik, R., Singh, J., Saxena, A.K., Srinivasan, R. & Raveendran, A.V., 1999, *Sol. Phys.*, 188, 89
13. Pasachoff, J.M., Badcock, B.A., Russell, K.D. & Seaton, D.B., 2002, *Sol. Phys.*, 207, 241
14. Phillips, K.J.H., Read, P., Gallagher P.T., Keenan, F. P., Rudawy, P., Rempelt, B., Berlicki, A., Buczylo, A., Diego, F., Barnsley, R., Smartt, R.N., Pasachoff, J.M., Badcock, B.A., 2000, *Sol. Phys.*, 193, 259.
15. Williams, D.R., Phillips, K.J.H., Rudawy P., Mathioudakis, M., Gallagher, P. T., O'Shea, E., Keenan, F. P., Read, P., Rempelt, B., 2001, *MNRAS*, 326, 428
16. Williams, D. R., Mathioudakis, M., Gallagher P.T., Phillips, K. J. H., McAteer, R. T. J., Keenan, F. P., Rudawy, P., Katsiyannis, A. C., 2002, *MNRAS*, 336, 747
17. Katsiyannis, A. C., Williams, D. R., McAteer, R. T. J., Gallagher, P. T., Keenan, F. P., Murtagh, F., 2003, *A&A*, 406, 709
18. Torrence & C., Compo, G.P., 1998, *Bull. Amer. Meteor. Soc.*, 79, 61
19. Gallagher, P.T., Phillips, K.J.H., Harra-Murnion, L.K., Baudin, F. & Keenan, F.P., 1999, *A&A*, 348, 251
20. Ireland, J., Walsh, R.W., Harrison, R.A. & Priest, E.R., 1999, *A&A*, 347, 355
21. Banerjee, D., O'Shea, E. & Doyle, J.G., 2000, *A&A*, 355, 1152
22. Starck, J.-L. & Murtagh, F., 2002, '*Astronomical Image and Data Analysis*', Springer-Verlag Berlin Heidelberg